International Journal of Hydrogen Energy 51 (2024) 1109–1118

Contents lists available at ScienceDirect

International Journal of Hydrogen Energy

journal homepage: www.elsevier.com/locate/he

Improved supercapacitor and oxygen evolution reaction performances of morphology-controlled cobalt molybdate

Schindra Kumar Ray *, Bishnu Prasad Bastakoti **

Department of Chemistry, North Carolina A & T State University, 1601 E Market St, Greensboro, NC, 27411, USA

ARTICLE INFO

Handling editor: Dr F Gallucci

Keywords:
$CoMoO_4$: hydrothermal
Morphology-controlled
Supercapacitor
OER

ABSTRACT

Herein, various morphologies (Bundle of rods, rods, nanoparticles, and umbra) of cobalt molybdate ($CoMoO_4$) were obtained by changing the pH (6, 7, 8, and 9) of the solutions during hydrothermal synthesis. The evolution mechanism of different morphologies was explained. These samples were used for supercapacitors and oxygen evolution reaction (OER) catalysts. The higher double-layer capacitance (464 mF cm^{-2}) was observed in $CoMoO_4$ nanoparticles. It demonstrated high specific capacitance (191 F/g at a current density of 1 A/g) and excellent cyclic stability performance (98 % retention capability after 2000 cycles) in the 3 M KOH solution. Furthermore, $CoMoO_4$ nanoparticles showed the lowest overpotential (200 mV at 10 mA/cm^2) and onset potential in linear sweep voltammetry polarization curves, superior turnover frequency (0.0095 s^{-1}), and low Tafel slopes (149 mV/dec) compared to other morphologies. According to chronoamperometry test, good electrochemical stability was noted in nanoparticles for 10 h towards OER. The higher energy storage and OER performances of $CoMoO_4$ nanoparticles were related to excellent oxidation/reduction/electron transfer abilities, great surface area, and rich active sites. Thus, these findings suggest that morphology controlled $CoMoO_4$ could be a great candidate for efficient supercapacitor electrode materials and OER catalysts.

1. Introduction

Due to the rapid progress of human civilization, sustainable and clean energy sources are highly demanded to overcome the energy shortage in the world [1–3]. It can be achieved by the development of energy sources with storage technologies. Supercapacitors have attracted significant attention in energy storage technologies because of their high-power density, long cycle life, short discharging time, and low maintenance cost [4–6]. In addition, oxygen evolution reaction (OER) plays a significant role in the production of chemical fuels which is one of the environmentally friendly renewable energy sources [7,8]. The electrode materials have a crucial role in supercapacitors (SCs) and OER [9–11]. Due to the stable crystal structure, excellent redox behavior, notable physical/chemical properties, and superior electronic conductivity, metal molybdate compounds have been considered efficient electrode materials [12]. Cobalt molybdate ($CoMoO_4$) is a great candidate among them for SCs and OER due to low-priced, natural abundance, a great combination of high specific capacitance of cobalt oxide with rich polymorphisms of molybdenum oxide, multiple redox reactions, and outstanding chemical stability [13,14]. However, this electrode material suffers from slow electrochemical kinetics and low-rate capability [12,15].

To overcome these issues, researchers modify the electrode materials in several ways such as tuning of morphology, deposition of metal ions, and fabrication of composite structures with metal oxide/polymer/MOF/carbon, and doping of metals/non-metals [16–23]. Among these strategies, morphology-controlled is a low-cost technique *via* a change in solution properties such as acidity/basicity of precursors because it can alter the nucleation rate, growth of the crystal, and crystallinity [24–26]. It also provides active/reactive sites for enhancing the electron-transfer ability, specific surface area, great electrochemical kinetics, rate capability, short diffusion pathways for electrons/ions, improvement of diffusivity, and optimizations of the crystallinity/defects that enhance SCs and OER performances [21,27–32]. Even though many studies using different $CoMoO_4$ morphologies for energy storage and OER have been published, there are still many ways to tune the morphologies of the catalysts to enhance their performance. So, tuning the morphology of $CoMoO_4$ *via* changing the pH of the

* Corresponding author.
** Corresponding author.
E-mail addresses: schindrakumarray@gmail.com (S.K. Ray), bpbastakoti@ncat.edu (B.P. Bastakoti).

https://doi.org/10.1016/j.ijhydene.2023.11.003
Received 7 August 2023; Received in revised form 14 October 2023; Accepted 1 November 2023
Available online 10 November 2023

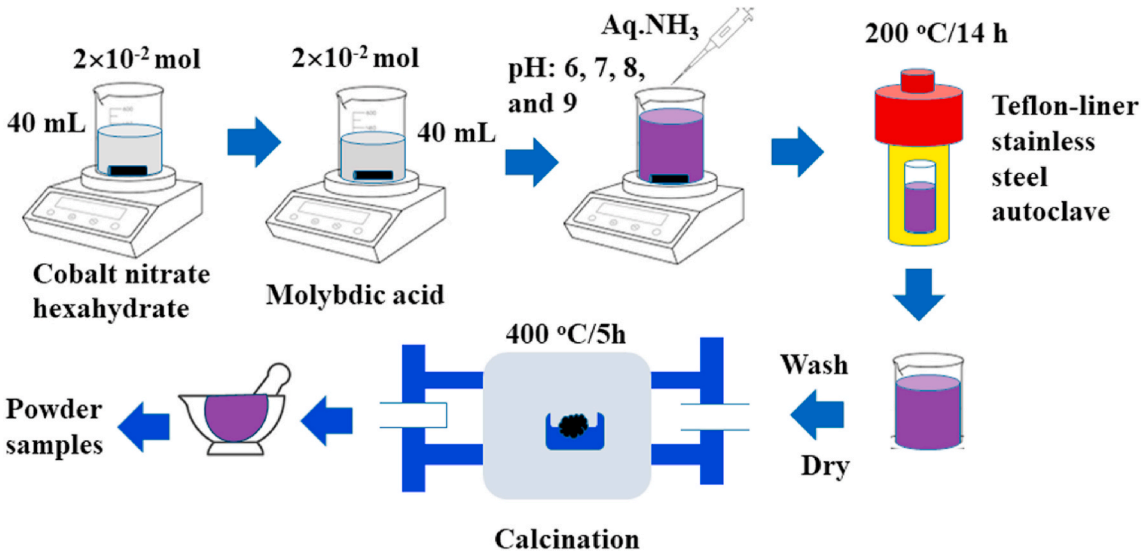

Fig. 1. Schematic illustration of synthesis procedure for $CoMoO_4$.

solution is a perfect option to increase the SCs and OER efficiencies.

Herein, various morphologies (bundle of nanorods, rods, nanosphere, and umbra) of $CoMoO_4$ were synthesized by hydrothermal process. The electrode materials were well characterized by X-ray diffraction (XRD), field emissions scanning electron microscopy (FESEM), transmission electron microscopy (TEM), energy-dispersive X-ray spectroscopy (EDS), Brunauer–Emmett–Teller (BET), X-ray photoelectron spectroscopy (XPS), and Raman spectroscopy. The mechanism related to the evolution of different morphologies was explained. The electrochemical performances of electrode materials were analysed by cyclic voltammetry (CV), electrochemical impedance spectroscopy (EIS), galvanostatic charge-discharge (GCD), cyclic stability, linear sweep voltammetry (LSV), and Tafel curves measurements for SCs and OER evaluation of electrode materials. In addition, turnover number (TON) and turnover frequency (TOF), and overpotential were investigated. The mechanism related SCs/OER analysis and stability were described.

2. Experimental section

2.1. Material synthesis

In this study, molybdic acid (H_2MoO_4), cobalt nitrate hexahydrate [$Co(NO_3)_2.6H_2O$], and aqueous ammonia (aq. NH_3) were used to synthesize the $CoMoO_4$ samples. These chemicals were purchased from Sigma-Aldrich and used without any further purification. 0.02 mol of Co $(NO_3)_2.6H_2O$ and H_2MoO_4 were separately dissolved in deionized water (40 mL) at room temperature. Then, the Co $(NO_3)_2.6H_2O$ solution was dropped to an H_2MoO_4 solution with constant stirring. After this mixing, the precipitate was formed and maintained at different pHs (6, 7, 8, and 9) using aq. NH_3. It was magnetically stirred for 4 h. The resulting solution was transferred into a Teflon-lined stainless autoclave which was kept for 14 h at 200 °C temperature. After hydrothermal treatment, the solution was washed multiple times with water and ethanol. It was dried in an oven at 80 °C. It was further calcined at 400 °C for 5 h. Finally, the powder samples were obtained which were grounded with the help of mortar/piston. All the samples were also prepared by the same techniques under similar conditions. For convenience, samples were coded as CM-B, CM-R, CM-N, and CM-U for pH 6, pH 7, pH 8, and pH 9, respectively. (B: bundles, R: rod, N: nanoparticle, U: umbra). The synthesis route of $CoMoO_4$ was schematically illustrated in Fig. 1.

2.2. Material characterization

The structural and morphological characterization of $CoMoO_4$ samples was investigated by field emission scanning electron microscopy (FESEM, JEOL, JSM-IT800). The energy dispersive X-ray spectrometry (EDS) and elemental mapping were measured on the Oxford instrument. Transmission electron microscopy (TEM), High-resolution transmission electron microscopy (HRTEM), selected area diffraction patterns (SAED) images were obtained by JEOL 1230. The crystal structures of powder samples were measured by X-ray diffractometer (XRD) (Rigaku, Miniflex 600) of Cu Kα radiation from 20 to 80°at a scanning speed of 1°/minute. The surface area of samples was investigated by using Brunauer–Emmett–Teller (BET) nitrogen adsorption method on Quanta Chrome. Before the surface area investigation, all the samples were degassed at 300 °C in a vacuum. X-ray photoelectron spectroscopy (XPS, Thermo Scientific ESCALAB™ XI, Al Kα/200 eV) was carried out. The Raman spectra of $CoMoO_4$ samples were investigated by using Horiba Raman Confocal Microscope. Calcination of samples was performed on a programmable furnace of MTI Corporation.

2.3. Electrochemical characterization

The electrochemical characterization was performed on a CH instrument based on a three-electrode system (working electrode: $CoMoO_4$, counter electrode: Pt, and reference electrode: Ag/AgCl-in 3 M KCl) using 3 M KOH. The working electrodes were prepared by making a slurry of the $CoMoO_4$ (4 mg) using 0.5 mL ethanol and 50 μL Nafion. The well-dispersed slurry was sonicated for 2 h. After that, it was placed in copper foil (2 cm × 2 cm) *via drop* casting method. The available working electrode was 1 cm^2. Then, it was dried at 80 °C for 4 h. Cyclic voltammetry (CV) was performed with a scan rate of 20–100 mV/s. The electrochemical impedance spectroscopy (EIS) with 0.1 Hz–100,000 Hz was measured. The specific capacitance of electrodes was calculated based on galvanostatic charge-discharge (GCD) measurements according to the equation:

$$C = I \times \Delta t/m \times \Delta V \quad \text{(i)}$$

Where I, m, Δt, and ΔV represent current (A), the mass of active materials (g), discharge time (s), and operating voltage (V) respectively [33]. The GCD stability of CM-N was performed for 2000 cycles. All potential measured were changed into reversible hydrogen electrode (RHE) scale using Nernst equation during linear sweep voltammetry (LSV) and Tafel measurements for oxygen evolution reaction using the following

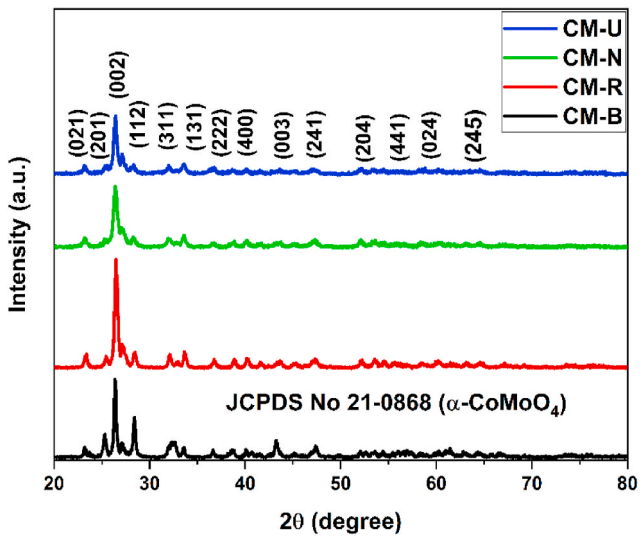

Fig. 2. XRD patterns of $CoMoO_4$ samples.

equation:

$$E_{RHE} = E_{Ag/AgCl} + 0.197 + 0.059\ pH \quad \text{(ii)}$$

Where $E_{Ag/AgCl}$ denotes potential against the reference electrode and 0.197 V shows the standard potential of Ag/AgCl at 25 °C [18]. LSV was performed in the range of 1–1.6 V vs RHE at a scan rate of 5 mV/s. The commercial RuO_2 (Thermo scientific) was used to compare the LSV of $CoMoO_4$ samples. The turnover frequency (TOF) of catalysts were calculated using formula:

$$TOF = TON/time = J \times A/4 \times F \times m \quad \text{(iii)}$$

Where J, A, F, m, and TON represent current density (A/cm^2) at an overpotential (η = 300 mV), surface area of the electrode, Faraday constant (96485 C/mol), number of moles of active metal on electrode, and turnover number respectively [34,35]. The stability of CM-N was investigated for 10 h through chronoamperometry test. CM-N was collected after stability 2000 cycles for supercapacitor and 10 h for OER. Then, it was washed with water and ethanol several times and dried. After that, XRD and FESEM measurements were performed.

3. Results and discussion

Fig. 2 revealed the XRD patterns of various $CoMoO_4$ samples. The diffraction peaks of samples were well matched with the monoclinic structure of α-$CoMoO_4$ (JCPDS no: 21–0868) [36]. It suggests the lowering of crystallinity with the increase in pH during the synthesis process. The possible reasons may associate with variations of the nucleation process that may change the crystallite structure [37]. The different intensities of XRD peaks showed the changes in the morphology/size of samples. Also, the position of (002) facet did not show any significant change. It suggests that $CoMoO_4$ lattice was not expand/-contract even formation of different morphologies/sizes of samples. Besides the XRD patterns of calcined samples, uncalcined samples were shown in Fig. S1. The XRD patterns of uncalcined $CoMoO_4$ samples also matched monoclinic structure of α-$CoMoO_4$. However, few peaks were appeared in samples which can be easily indexed as hydrate cobalt molybdate ($CoMoO_4.3/4H_2O$) [38,39]. It suggests that the XRD peaks related $CoMoO_4.3/4H_2O$ phase disappeared during calcination process and formation of pure $CoMoO_4$ phase.

As expected, when making different pH of the solution during the synthesis, many exciting morphologies appeared. The morphologies/sizes of samples were analysed by FESEM images (Fig. 3). CM-B, CM-R, CM-N, and CM-U revealed bundles of nanorod (100 nm–600 nm in length and 60 nm–150 nm in width), rods (1 μm–3 μm in length and 500 nm to 1 μm width), nanoparticles (50 nm–80 nm), and umbra (1 μm), respectively (Fig. 3a-d). To observe the effect of calcination on morphologies/sizes, FESEM images of uncalcined $CoMoO_4$ samples were analysed (Fig. S2). The morphologies of uncalcined samples were like that of the calcined samples. In addition, FESEM elemental mapping

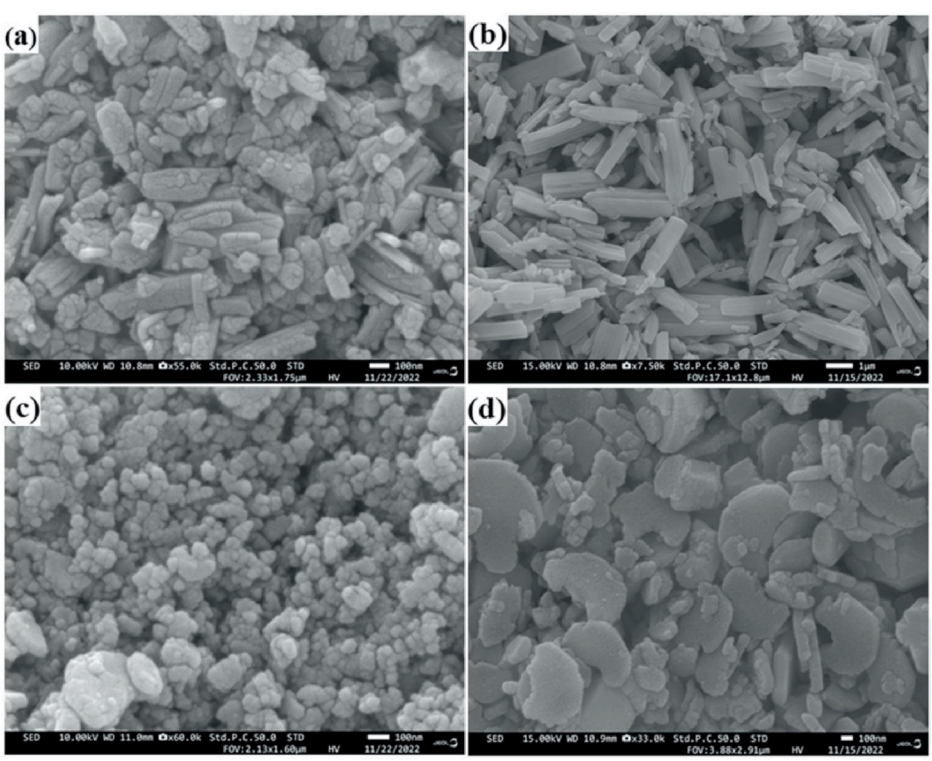

Fig. 3. FESEM images of the various $CoMoO_4$ samples. (a) CM-B, (b) CM-R, (c) CM-N, and (d) CM-U.

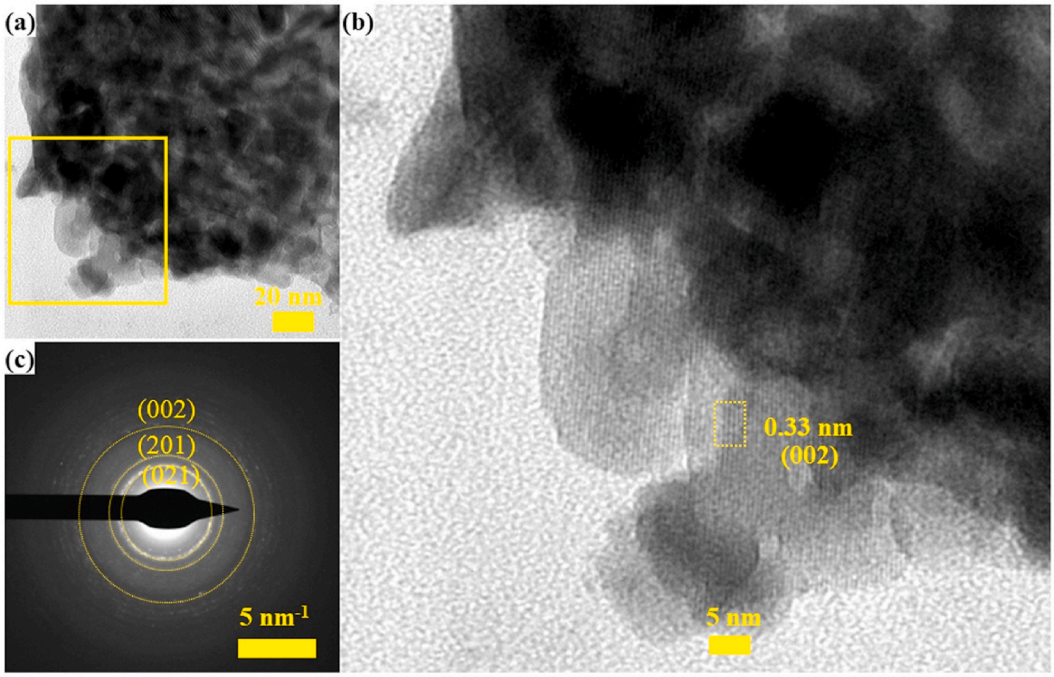

Fig. 4. (a) TEM, (b) magnified part of TEM image, and (c) SAED images of CM-N sample.

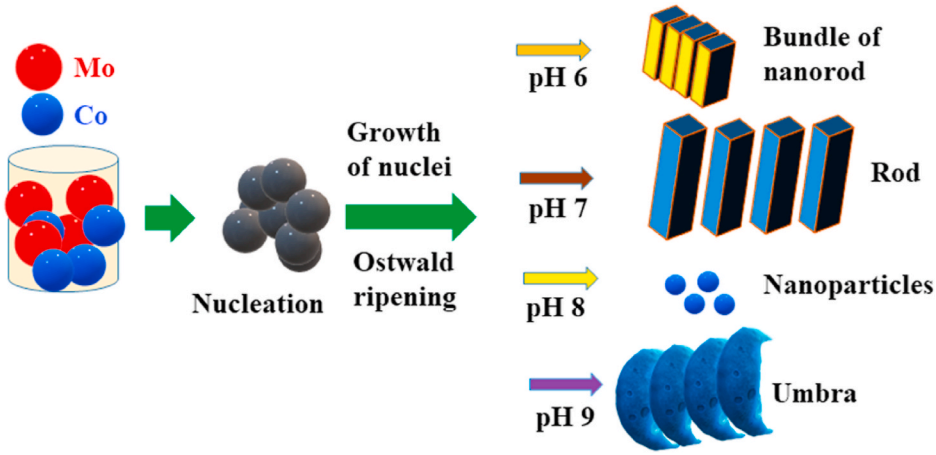

Fig. 5. Schematic formation mechanism of $CoMoO_4$ samples.

shows the homogenous distribution of Co, Mo, and O in samples (Fig. S3). The EDS of samples were presented in Fig. S4 (a, b, c, and d) that suggest the existence of Co, Mo, and O in samples.

The morphology of CM-N sample was further investigated by TEM and SAED analyses (Fig. 4). As shown in Fig. 4a, the TEM image of CM-N clearly revealed the nanoparticles. Fig. 4b revealed 0.33 nm lattice fringes corresponding to the (002) plane of $CoMoO_4$. Also, this plane was strongest peak in the XRD spectrum. According to Fig. 4c, All the interplanar spacing measured from the SAED patterns were consistent with the crystallographic plane of $CoMoO_4$. In addition, lattice fringes and the diffraction pattern suggested the crystalline nature of synthesized material.

The formation mechanisms for the evolution of different morphologies have been presented in Fig. 5. The crystal nucleation and growth were affected by altering the pH value of the precursor solution. At acidic conditions, the H^+ ion may attach the MoO_4^{2-} ions plane during the crystal growth initially because of electrostatic attraction that can affect the crystal nucleation process [26,40]. At pH 6, the nucleation rate was increased, and a huge number of $CoMoO_4$ were produced. In this process, $[Co(NH_3)_4]^{2+}$ intermediate may attach at the sites of $CoMoO_4$ single nuclei due to the existence of more growth sides [41]. So, the bundle of nanorods has appeared. However, there is a lack of growth sides in pH 7, and rods were formed. With the increase in pH value of the precursor solution, the crystal growth rate was increased, and the nucleation rate was decreased. Also, huge number of highly energetic nuclei may form. Due to these reasons, nanoparticles were observed at pH 8. In addition, nucleation, Ostwald ripening, and oriented attachment may produce umbra like structure [42].

XPS experiments were performed to know the information on the surface chemical compositions and oxidation states of the as-synthesized samples and the result is as displayed in Fig. 6. The XPS spectrum of Co 2p displayed four peaks that contain two spin orbit doublet characteristics of $2p_{3/2}$ (CM-B: 782.18 eV, CM-R: 782.71 eV, CM-N: 782.35 eV, and CM-U: 782.16 eV), satellite $2p_{3/2}$ (CM-B: 787.82 eV, CM-R: 787.05 eV, CM-N: 786.92 eV, and CM-U: 787.79 eV), $2p_{1/2}$ (CM-B: 798.24 eV, CM-R: 797.74 eV, CM-N: 798.28 eV, and CM-U: 798.79 eV), and satellite

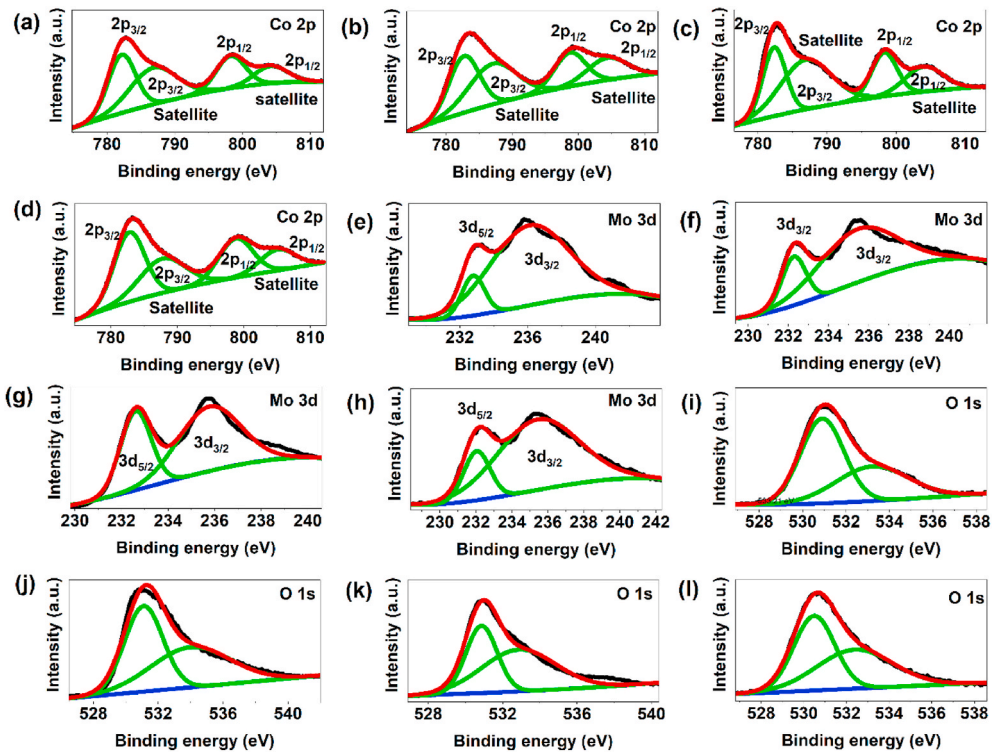

Fig. 6. XPS of CM-B (a, e, and i) CM-R (b, f, and j), CM-N (c, g, and k), and CM-U (d, h, and l).

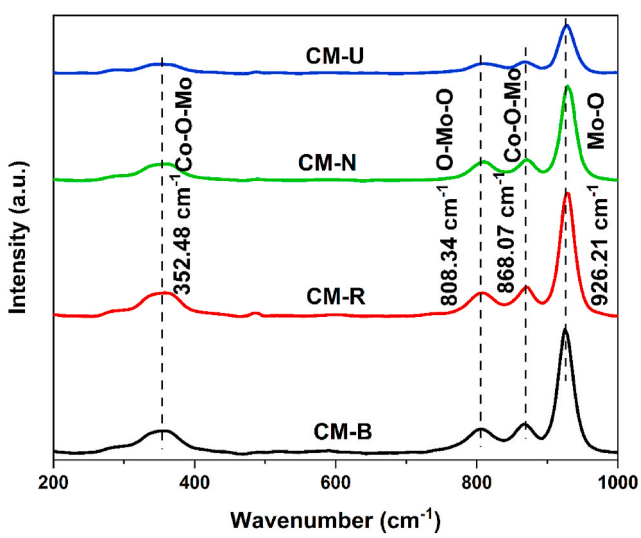

Fig. 7. Raman spectra of $CoMoO_4$ samples.

$2p_{1/2}$ (CM-B: 804.16 eV, CM-R: 804.36 eV, CM-N: 804.03 eV, and CM-U: 805.07 eV) (Fig. 6a-d). These peaks indicate the existence of Co^{2+} in the sample [43]. The Mo 3d spectrum of samples showed a spin orbit doublet Mo $3d_{5/2}$ (CM-B: 232.99 eV, CM-R: 231.93 eV, CM-N: 232.61 eV, and CM-U: 232.17 eV) and Mo $3d_{3/2}$ (CM-B: 235.82 eV, CM-R: 234.99 eV, CM-N: 235.76 eV, and CM-U: 235.14 eV) (Fig. 6a-d). It demonstrates the existence of Mo^{6+} in the samples [44]. As shown in Fig. 6i–l, two peaks of O 1s showed O^{2-} species in lattice CM-B: 530.90 eV, CM-R: 531.10 eV, CM-N: 530.86 eV, and CM-U: 530.49 eV) and chemisorbed or dissociated oxygen species (CM-B: 533.21 eV, CM-R: 533.99 eV, CM-N: 532.87 eV, and CM-U: 532.39 eV), respectively [45]. These XPS results suggest that oxidation state of samples was unaffected by different morphologies/sizes. Furthermore, Fig. S5 revealed Co 2p, Mo 3d, O 1s, and O Auger in the survey XPS spectrum, suggesting the co-existence of Co, Mo, and O elements in samples [46].

Fig. 7 presented the Raman spectra of $CoMoO_4$ samples at room temperature. The vibrational modes were observed at 926.21, 868.07, 808.34, and 352.48 cm^{-1}. The frequency observed at 926.51 cm^{-1} was assigned with a symmetric stretching mode of doubly coordinated bridging oxygen (Mo–O) [47]. The symmetric stretching of Co–O–Mo (868.07 cm^{-1}) was found. In addition, the band located at 808.34 cm^{-1} can be associated with the asymmetric stretching mode of oxygen (O–Mo–O) [48]. Also, symmetry bending mode (O–Mo–O) was noted at 352.48 cm^{-1} [13]. It has been found that the intensity of Raman peaks was decreased with an increase in the pH of samples during the synthesis process. The highest intensity was found in CM-B whereas the lowest intensity was noted in CM-U. The variation of peak intensity of $CoMoO_4$ samples and slight shift in Raman peaks may be associated with crystallinity, size/morphology, and structural order/disorder in the lattice [49,50]. It also suggests that monoclinic structure of α-$CoMoO_4$ was not damaged during tuning the different morphologies/sizes. The Raman spectroscopy of $CoMoO_4$ samples were in line with XRD results. It means that $CoMoO_4$ samples did not contain phases other than those shown by XRD.

The specific surface area of the sample is one of the important parameters that determine the electrochemical performance. As shown in Fig. S6 (a, b, c, and d), the isotherm of samples presented type IV with H3 -type hysteresis loops. The BET surface area of the CM-B, CM-R, CM-N, and CM-U were calculated to be 14.39, 23.93, 50.372, and 4.53 m^2/g respectively. The specific surface area of CM-N demonstrated a higher surface area than others. According to Fig. S7 (a, b, c, and d), the intense peaks in the pore size distribution of samples were observed at 18.30, 10.36, 11.09, and 7.93 nm for CM-B, CM-R, CM-N, and CM-U, respectively. Also, a few macropores were noted in the samples. The large specific surface area and abundant mesoporous structure could boost the contact area between the electrode and electrolyte, leading to creating enough active sites for redox reactions as well as great transport of electrons/ions [51,52]. Therefore, the superior BET surface area and mesopore structure of CM-N might reveal better electrochemical

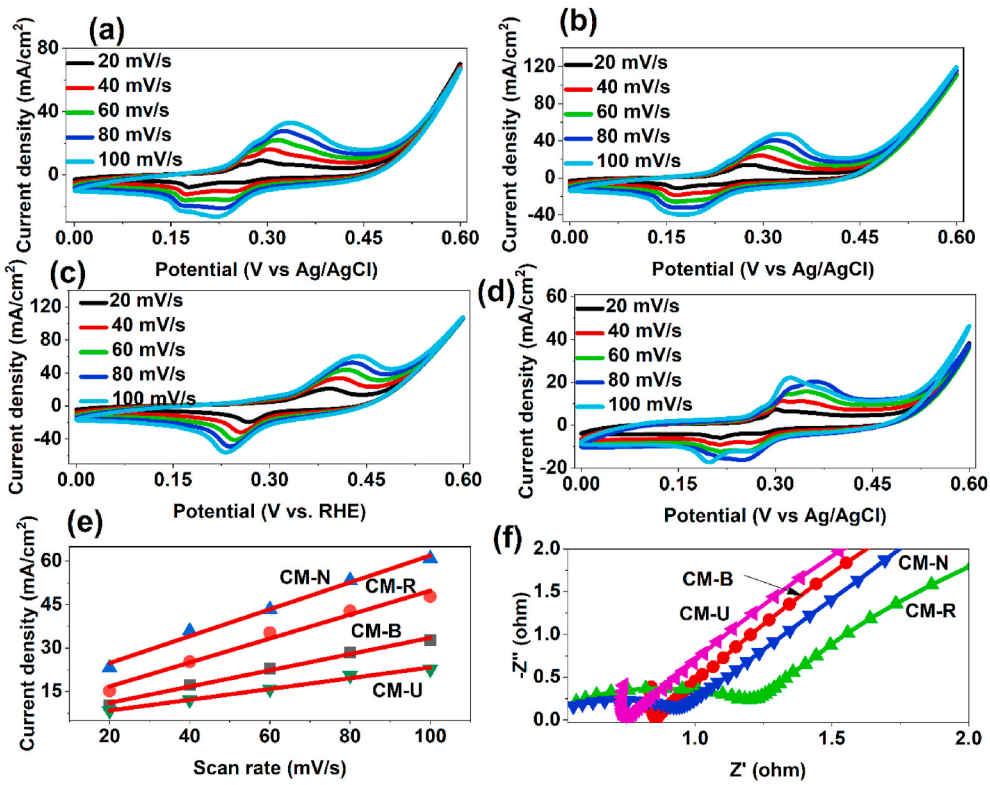

Fig. 8. CV (a: CM-B, b: CM-R, c: CM-N, and d: CM-U), current density as a function of scan rate (e), and EIS (f) of $CoMoO_4$ samples.

performance than other samples.

The electrochemical measurements were conducted to analyze the pseudocapacitive properties of $CoMoO_4$ electrodes (Fig. 8) The CV graphs of the various morphologies of $CoMoO_4$ electrodes under the different scan rates (20 mV/s, 40 mV/s, 60 mV/s, 80 mV/s, and 100 mV/s) in 3 M KOH electrolyte with potential ranges from 0 to 0.6 V (vs. Ag/AgCl) are presented in Fig. 8a-d. All the curves reveal similar shapes. In addition, the typical Faradic reaction peaks can be clearly observed in all samples that suggest the pseudocapacitor electrodes. The formation of redox peaks is related to the charge-transfer kinetics of Co^{2+}/Co^{3+} and OH^- ions of electrolyte. During this redox reaction, $CoMoO_4$ interacts with OH^- ions to form CoOOH, MoO_3, CoO_2, and H_2O. CoOOH further reacts with H_2O to produce $Co(OH)_2$ [51].

The shifting of redox peaks from higher to lower potential and an increase in the potential difference between oxidation/reduction peaks were observed with an increased scan rate. It also suggests the enhancement of the irreversible degree and the quasi-reversible reaction with the increment of scan rate. These may be associated with the internal resistance of the $CoMoO_4$ electrodes and the polarization in a high scan rate [51]. The integral area of CM-N was evidently higher than CM-B, CM-R, and CM-U (CM-N > CM-R > CM-B > CM-U), suggesting larger specific capacitance and better electrochemical performance (Fig. 8a–d and S8). The enhanced performance of the CM-N might be due to a larger surface area and better pore size than others that can expose a higher number of active sites for ion intercalation [53]. The electrochemical surface area (ECSA) was estimated by double-layer capacitance (C_{dl}) via CV at various scan rates from 20 to 100 mV/s (Fig. 8e). The C_{dl} value of CM-N is 464 mF cm^{-2} which is higher than those of CM-B (280 mF cm^{-2}), CM-R (413 mF cm^{-2}), and CM-U (186 mF cm^{-2}). The higher ESCA provides the exposure of more active surfaces for superior electrocatalytic performances [54].

To determine the electron transfer kinetics at the $CoMoO_4$-electrolyte surface, the EIS of the sample was measured (Fig. 8f). Nyquist plots obtained from EIS revealed that samples have a semicircle in the high-frequency region as well a as straight line in the low-frequency region. The arc CM-N showed smaller semicircles or low impedance which is more beneficial for electrolyte ion diffusion/charge transfer [55]. In addition, the equivalent circuit was shown in Fig. S9. The collected values of solution resistance (R1), charge transfer resistance (R2), electric double layer capacitance (C2), Warburg coefficient (σ), and constant phase element (Q) were listed in Table S1. It suggests the lower charge transfer resistance in CM-N that indicates the better electrocatalytic property of nanoparticles.

To further explore the electrochemical behavior of $CoMoO_4$, GCD measurements were carried out at various current densities (1, 1.25, 1.5, and 2 A/g) which are shown in Fig. 9a-d. CM-N electrode displayed the longest GCD time as compared to CM-B, CM-R, and CM-U electrodes, which is in good agreement with CV and EIS. Among the other materials, CM-N displayed outstanding specific capacitance with 191 F/g at a current density of 1 A/g. The specific capacitance of $CoMoO_4$ samples was calculated and shown in Table S2. It suggests that nanoparticles enhanced specific capacitance by three folds than others (bundle of rods, rod, and umbra). The possible reasons may relate to a large specific surface area and multiple active sites that can provide electrons for charge storage/delivery, great electrochemical active area for a redox reaction, thereby enhancing the electrical conductivity as well as diffusion kinetics.

For practical supercapacitor application of materials, the cyclic stability was evaluated (Fig. 10). The GCD tests over 2000 cycles were performed for CM-N at a current density of 1 A/g. Fig. S10 presented the first and last cycles of GCD performance of cyclic stability tests of $CoMoO_4$ nanoparticles. Interestingly, the results demonstrate about 98 % retention in capacitance over 2000 cycles at 1 A/g. Also, the EIS plots of CM-N after 2000 cycles revealed evidence of stability (Fig. S11). The XRD pattern and FESEM image of CM-N after GCD cycling were like that of a fresh sample indicatinggreat stability of $CoMoO_4$ electrode under basic conditions that revealed the excellent supercapacitance behavior along with long cycle durability (Figs. S12 and S13). The specific capacitance and retention are comparable with previously reported literature (Table 1). This Table also demonstrated the fabrication of

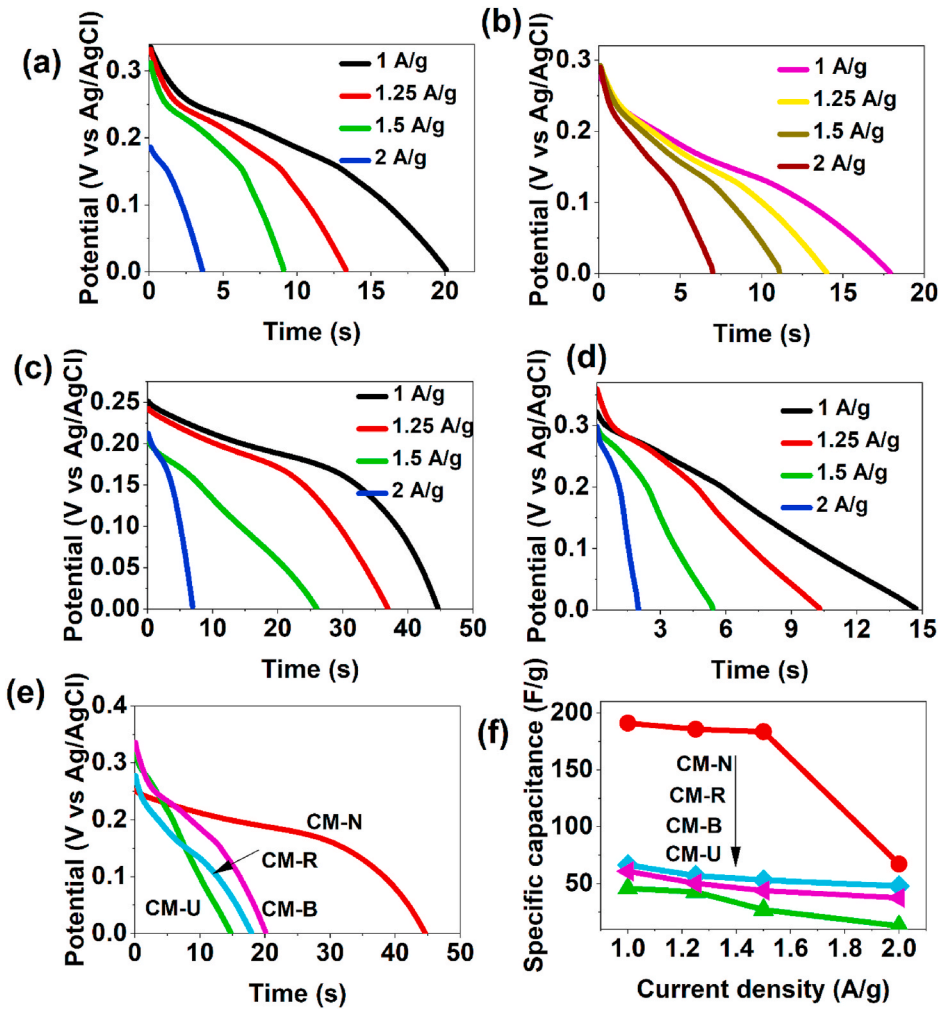

Fig. 9. GCD and specific capacitance graphs of $CoMoO_4$ samples. a) CM-B, (b) CM-R, (c) CM-N, (d) CM-U, (e) GCD comparison, (f) specific capacitance.

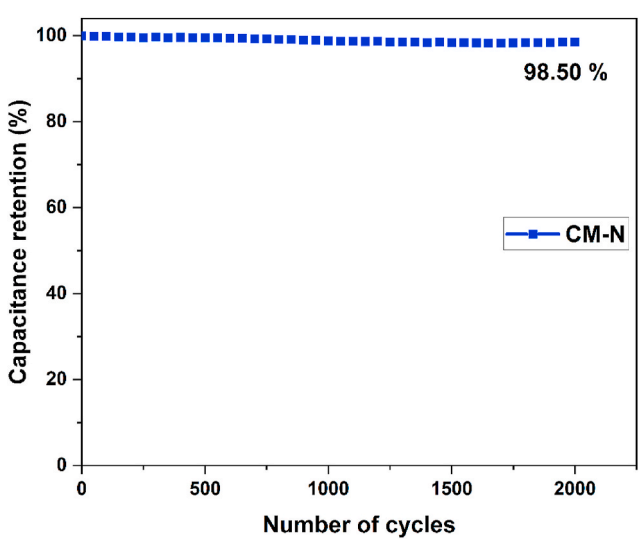

Fig. 10. Cyclic stability of CM-N sample after 2000 cycles.

different morphologies by various synthesis methods (hydrothermal, microwave irradiation, combustion, and co-precipitation) for energy storage applications.

The application of different morphologies of $CoMoO_4$ electrodes as

Table 1
Comparison of specific capacitance and retention percentage of $CoMoO_4$ based on published literatures.

Synthesis technique	Morphology	Specific capacitance	Capacitance retention	Ref
Hydrothermal and calcination	Microsphere	186 F/g at 1A/g	45 % for 1000 cycles	[51]
Microwave irradiation	Nanoplatelets	95 F/g	–	[56]
Hydrothermal	Nanorod	123 F/g at 1 mA/cm^2	83 % for 3000 cycles	[57]
Combustion	Granular	105 F/g at 1A/g	86 % for 4000 cycles	[58]
Microwave combustion	Nanorod	133 F/g at 1 mA/cm^2	100 % for 1000 cycles	[59]
Co-precipitation	Nanorod	114 F/g at 0.5 A/g	81 % for 3000 cycles	[60]
Co-precipitation	Rice and irregular	180 F/g at 1 mA/cm^2	83 % for 5000 cycles	[36]
Combustion	Irregular	40 F/g at 1 A/g	60 % for 2000 cycles	[61]
Hydrothermal and calcination	Bundle of nanorods, rod, nanoparticles, and umbra	191 F/g at 1A/g	98 % for 2000 cycles	Our work

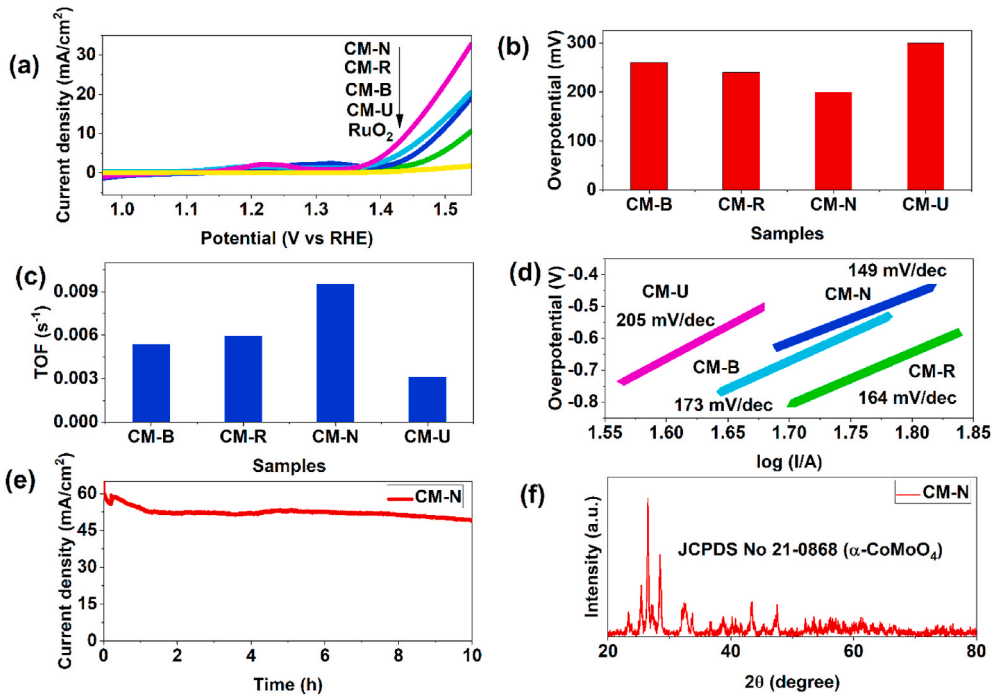

Fig. 11. (a) LSV, (b) overpotential required for current density at 10 mA/cm^2, (c) TOF, (d) Tafel plots, (e) j–t curve at a constant potential of 0.6 V for 10 h and (f) XRD pattern after 10 h of $CoMoO_4$ samples.

an OER electrocatalyst was evaluated in 3 M KOH using a standard three-electrode system (Fig. 11). Commercial RuO_2, CM-B, CM-R, CM-N, and CM-U were measured under the similar conditions for comparison. According to LSV polarization curve, the peaks at ~1.25–1.35 versus RHE suggested the oxidation of Co^{2+} to Co^{2+} and Co^{4+} oxidation states in $CoMoO_4$ samples (Fig. 11a) [20]. The strong Co^{2+} oxidation peaks indicate the existence of active sites for OER in an alkaline solution. Also, the lowest onset potential was seen in the CM-N sample as compared to CM-B, CM-R, CM-U, and commercial RuO_2. The higher OER performance of nanoparticles may be associated with a rich conductive porous structure with a great surface area that permits acceleration on the catalytic surface. For a detailed analysis of LSV, the overpotentials of different catalyst at current densities of 10 mA/cm^2 was presented in Fig. 11b. At the current density of 10 mA/cm^2, the nanoparticles CM-N catalyst only required 200 mV, which is lower than other catalysts (CM-B: 260 mV, CM-R: 240 mV, and CM-U: 300 mV). The lower overpotential of CM-N suggested the superior OER efficiency than others. Furthermore, TOF analysis was used to observe the intrinsic OER performance of samples (Fig. 11c). The results clearly suggests that CM-N is the most active OER $CoMoO_4$ catalyst with the highest TOF of 0.0095 s^{-1}, which is higher than those of CM-B (0.0053 s^{-1}), CM-R (0.0059 s^{-1}), and CM-U (0.0031 s^{-1}).

To evaluate the kinetics of OER for $CoMoO_4$ samples, Tafel plot was measured (Fig. 11d). The OER in $CoMoO_4$ is originated by the internal redox process and formation of CoOOH [62]. The Tafel slope of CM-N is only 149 mV/dec, while that of others (CM-B: 173 mV/dec, CM-R: 164 mV/dec, and CM-U: 205 mV/dec) are high, indicating that the formation of nanoparticles enhances the OER electrocatalytic activity/kinetic, and $CoMoO_4$ nanoparticles have better OER activity than others. The stability is key index to evaluate the performance of catalyst for OER performance. The stability of CM-N was tested in 3 M KOH for 10 h at a current density of 50 mA/cm^2 through chronoamperometry test (Fig. 11e). The current density has no obvious decline, indicating a good stability of CM-N. Meanwhile, no observable changes in XRD patterns and morphology of CM-N after 10 h stability test, suggesting the strong electrochemical stability of the catalyst towards OER (Fig. 11f and S14). Beside stability, TON is also one of the important factor for evaluation of catalyst for industrial application. TON of CM-N revealed 3.42 × 10^3 that shows the good catalytic performances for OER activity. The OER activity comparison of the as-synthesized sample with other

Table 2
The OER performances of recent report on $COMoO_4$-based catalysts.

Catalysts	Preparation method	Electrolytes	Overpotential 10 mA cm^{-2}/V	Tafel slop (mV dec-1)	Stability	Ref.
$CoMoO_4$ nanostructures	Solvothermal	1 M KOH	254 mV	58	16 h	[63]
$CoMoO_4$ nanotubes	Calcination	1 M KOH	315 mV	89	20 h	[64]
C-coated Co_3O_4/$CoMoO_4$ hollow sphere	Carbonization and calcination	1 M KOH	410 mV	84	5 h	[65]
$CoMoO_4$ flake	Hydrothermal	1 M KOH	322 mV	103.5	12 h	[66]
F–$CoMoO_{4-x}$@GF	Hydrothermal	–	246 mV	64.4	20 h	[67]
Mo_1–CoOOH@CP	Scalable Pyrolysis	1 M KOH	274 mV	66	100 h	[68]
$CoMoO_4$@$_{Co1.62}Mo_6S_8$	Chemical vapor deposition and hydrothermal	1 M KOH	200 mV	59.34	14 h	[69]
CoP@$CoMoO_4$ hollow nanotube	sublimation- vapor phase transformation	1 M KOH	120 mV	91	24 h	[54]
Ni–$CoMoO_4$	Reflux	1 M KOH	291 mV	57	50 h	[70]
$CoMoO_4$ nanostructures	hydrothermal	3 M KOH	200 mV	149	10 h	Our work

$CoMoO_4$-based materials was listed in Table 2. It is found that our results are comparable as compared to previous literatures.

4. Conclusions

In summary, various morphologies/sizes of $CoMoO_4$ (bundle of nanorods, rods, nanoparticles, and umbra) were synthesized by hydrothermal method *via* the change in pH of the solution during synthesis. The as-prepared materials were well characterized by various techniques, and electrochemical measurements were carried out for supercapacitors and OER. The electrochemical performance of samples has been found in the following order: nanoparticles > rods > bundle of nanorods > umbra. The $CoMoO_4$ nanoparticles revealed a high specific capacitance of 191 F/g at 1A/g and superior stability (98 % retention after 2000 cycles). Low overpotential, small Tafel slope, great turnover frequency/number, and good electrochemical stability of samples suggest suitable OER catalysts. In conclusion, tuning of $CoMoO_4$ morphology is a perfect way to make bifunctional electrocatalysts for efficient supercapacitor and OER.

Declaration of competing interest

The authors declare that they have no known competing financial interests or personal relationships that could have appeared to influence the work reported in this paper.

Acknowledgments

This work was financially supported by the National Science Foundation Research Initiation Award (NSF-RIA 2000310). Part of the work was also supported by NSF Partnerships for Research and Education in Materials (NSF-PREM 2122067). The samples were characterized in the Joint School of Nanoscience and Nanoengineering, a member of the Southeastern Nanotechnology Infrastructure Corridor and National Nanotechnology Coordinated Infrastructure, which is supported by the National Science Foundation (Grant ECCS-1542174). The authors thank Dr. Debasish Kuila's group at North Carolina A&T State University for BET measurements. The Authors also thank Mr. Rabin Dahal for SEM imaging and Mr. Moses Ashie for Raman and XPS measurements.

Appendix A. Supplementary data

Supplementary data to this article can be found online at https://doi.org/10.1016/j.ijhydene.2023.11.003.

References

[1] Wang G, Zhang L, Zhang J. A review of electrode materials for electrochemical supercapacitors. Chem Soc Rev 2012;41:797–828. https://doi.org/10.1039/c1cs15060j.
[2] Liu C, Li F, Lai-Peng M, Cheng HM. Advanced materials for energy storage. Adv Mater 2010;22:28–62. https://doi.org/10.1002/adma.200903328.
[3] Tong R, Xu M, Huang H, Wu C, Luo X, Cao M, et al. 3D V–Ni3S2@CoFe-LDH core-shell electrocatalysts for efficient water oxidation. Int J Hydrogen Energy 2021;46:39636–44. https://doi.org/10.1016/j.ijhydene.2021.09.190.
[4] Nandi D, Mohan VB, Bhowmick AK, Bhattacharyya D. Metal/metal oxide decorated graphene synthesis and application as supercapacitor: a review. J Mater Sci 2020;55:6375–400. https://doi.org/10.1007/s10853-020-04475-z.
[5] Poonam Sharma K, Arora A, Tripathi SK. Review of supercapacitors: materials and devices. J Energy Storage 2019;21:801–25. https://doi.org/10.1016/j.est.2019.01.010.
[6] Rehman J, Eid K, Ali R, Fan X, Murtaza G, Faizan M, et al. Engineering of transition metal sulfide nanostructures as efficient electrodes for high-performance supercapacitors. ACS Appl Energy Mater 2022;5:6481–98. https://doi.org/10.1021/acsaem.1c03937.
[7] Li J. Oxygen evolution reaction in energy conversion and storage: design strategies under and beyond the energy scaling relationship, vol. 14. Springer Nature Singapore; 2022. https://doi.org/10.1007/s40820-022-00857-x.
[8] Eid K, Sliem MH, Abdullah AM. Tailoring the defects of sub-100 nm multipodal titanium nitride/oxynitride nanotubes for efficient water splitting performance. Nanoscale Adv 2021;3:5016–26. https://doi.org/10.1039/d1na00274k.
[9] Ipadeola AK, Haruna AB, Gaolatlhe L, Lebechi AK, Meng J, Pang Q, et al. Efforts at enhancing bifunctional electrocatalysis and related events for rechargeable zinc-air batteries. Chemelectrochem 2021;8:3998–4018. https://doi.org/10.1002/celc.202100574.
[10] Ibrahim Y, Mohamed A, Abdelgawad AM, Eid K, Abdullah AM, Elzatahry A. The recent advances in the mechanical properties of self-standing two-dimensional MXene-based nanostructures: deep insights into the supercapacitor. Nanomaterials 2020;10:1–27. https://doi.org/10.3390/nano10101916.
[11] Zhang L, Zhao H, Xu S, Liu Q, Li T, Luo Y, et al. Recent advances in 1D electrospun nanocatalysts for electrochemical water splitting. Small Struct 2021;2:2000048. https://doi.org/10.1002/sstr.202000048.
[12] Zhang L, Zheng S, Wang L, Tang H, Xue H, Wang G, et al. Fabrication of metal molybdate micro/nanomaterials for electrochemical energy storage. Small 2017;13:1–19. https://doi.org/10.1002/smll.201700917.
[13] Fang L, Wang F, Zhai T, Qiu Y, Lan M, Huang K, et al. Hierarchical CoMoO4 nanoneedle electrodes for advanced supercapacitors and electrocatalytic oxygen evolution. Electrochim Acta 2018;259:552–8. https://doi.org/10.1016/j.electacta.2017.11.012.
[14] Jiang S, Pang M, Pang M, Song J, Wang R, Yang H, et al. 3D emerging nanosheets comprising hierarchical CoMoO4/MnO2 composites for flexible all-solid-state asymmetric supercapacitors. Colloids Surf A Physicochem Eng Asp 2023;656:130536. https://doi.org/10.1016/j.colsurfa.2022.130536.
[15] Prabhu S, Gowdhaman A, Harish S, Navaneetham M, Ramesh R. Synthesis of petal-like CoMoO4/r-GO composites for high performances hybrid supercapacitor. Mater Lett 2021;295:129821. https://doi.org/10.1016/j.matlet.2021.129821.
[16] Li L, Zhang L, Gou L, Wei S, Hou X, Wu L. High-performance methanol electrolysis towards energy-saving hydrogen production: using Cu2O-Cu decorated Ni2P nanoarray as bifunctional monolithic catalyst. Chem Eng J 2023;454. https://doi.org/10.1016/j.cej.2022.140292.
[17] Chen ZY, Liu H, Zhang LC, Li QL, Xu MW, Bao SJ. Facile and scale synthesis of Co/N/S-doped porous graphene-like carbon architectures as electrocatalysts for sustainable zinc-air battery cells. ACS Sustainable Chem Eng 2019;7:7743–9. https://doi.org/10.1021/acssuschemeng.8b06634.
[18] Ahsan MA, He T, Eid K, Abdullah AM, Sanad MF, Aldalbahi A, et al. Controlling the interfacial charge polarization of MOF-derived 0D–2D vdW architectures as a unique strategy for bifunctional oxygen electrocatalysis. ACS Appl Mater Interfaces 2022;14:3919–29. https://doi.org/10.1021/acsami.1c17283.
[19] Zhang D, Cao J, Zhang X, Zeng Z, Insin N, Qin J, et al. Modification strategies of layered double hydroxides for superior supercapacitors. Adv Energy Sustain Res 2022;3:2100183. https://doi.org/10.1002/aesr.202100183.
[20] Tantraviwat D, Anuchai S, Ounnunkad K, Saipanya S, Aroonyadet N, Rujijanagul G, et al. Structural properties of tungsten-doped cobalt molybdate and its application in electrochemical oxygen evolution reaction. J Mater Sci Mater Electron 2018;29:13103–11. https://doi.org/10.1007/s10854-018-9432-2.
[21] Wang F, Zhao J, Tian W, Hu Z, Lv X, Zhang H, et al. Morphology-controlled synthesis of CoMoO 4 nanoarchitectures anchored on carbon cloth for high-efficiency oxygen oxidation reaction. RSC Adv 2019;9:1562–9. https://doi.org/10.1039/c8ra09484e.
[22] Shaheen Shah S, Abu Nayem SM, Sultana N, Saleh Ahammad AJ, Abdul Aziz M. Preparation of sulfur-doped carbon for supercapacitor applications: a review. ChemSusChem 2022;15. https://doi.org/10.1002/cssc.202101282.
[23] Zhang Z, Cheng Y, Li H, Xu Z, Sun S, Yin S. Construction of Cu-doped Ni-Co-based electrodes for high-performance supercapacitor applications. ACS Appl Energy Mater 2022;5:6642–53. https://doi.org/10.1021/acsaem.2c00079.
[24] Ray SK, Hur J. A review on monoclinic metal molybdate photocatalyst for environmental remediation. J Ind Eng Chem 2021;101:28–50. https://doi.org/10.1016/j.jiec.2021.06.027.
[25] Ray SK, Hur J. A critical review on modulation of NiMoO4-based materials for photocatalytic applications. J Environ Manag 2021;278:111562. https://doi.org/10.1016/j.jenvman.2020.111562.
[26] Ray SK, Dhakal D, Lee SW. Insight into malachite green degradation, mechanism and pathways by morphology-tuned α -NiMoO 4 photocatalyst. Photochem Photobiol 2018;94:552–63. https://doi.org/10.1111/php.12872.
[27] Li YF. First-principles simulations for morphology and structural evolutions of catalysts in oxygen evolution reaction. ChemSusChem 2019;12:1846–57. https://doi.org/10.1002/cssc.201802525.
[28] Ma Y, Hou C, Zhang H, Qiao M, Chen Y, Zhang H, et al. Morphology-dependent electrochemical supercapacitors in multi-dimensional polyaniline nanostructures. J Mater Chem A 2017;5:14041–52. https://doi.org/10.1039/c7ta03279j.
[29] Lu Y, Zhang S, Han X, Wan X, Gao J, Bai C, et al. Controlling and optimizing the morphology and microstructure of 3D interconnected activated carbons for high performance supercapacitors. Nanotechnology 2021;32. https://doi.org/10.1088/1361-6528/abc98d.
[30] Wang DG, Wang H, Lin Y, Yu G, Song M, Zhong W, et al. Synthesis and morphology evolution of ultrahigh content nitrogen-doped, micropore-dominated carbon materials as high-performance supercapacitors. ChemSusChem 2018;11:3932–40. https://doi.org/10.1002/cssc.201801892.
[31] Dar FI, Moonooswamy KR, Es-Souni M. Morphology and property control of NiO nanostructures for supercapacitor applications. Nanoscale Res Lett 2013;8:1–7. https://doi.org/10.1186/1556-276X-8-363.
[32] Banerjee AN, Anitha VC, Joo SW. Improved electrochemical properties of morphology-controlled titania/titanate nanostructures prepared by in-situ hydrothermal surface modification of self-source Ti substrate for high-performance supercapacitors. Sci Rep 2017;7:1–20. https://doi.org/10.1038/s41598-017-11346-2.

[33] Ray SK, Pant B, Park M, Hur J, Lee SW. Cavity-like hierarchical architecture of WS2/α-NiMoO4 electrodes for supercapacitor application. Ceram Int 2020;46: 19022. https://doi.org/10.1016/j.ceramint.2020.04.232. –7.
[34] Huang S, Lu J, Wu X, Zhu H, Shen X, Cui S, et al. Ru-promoted NiFe oxyhydroxide anchored on the hierarchical porous N-doped carbon aerogel: electronic structures modulation for much enhanced OER/HER dual-functional characteristics. Appl Catal Gen 2023;664:119331. https://doi.org/10.1016/j.apcata.2023.119331.
[35] Kozuch S, Martin JML. "Turning over" definitions in catalytic cycles. ACS Catal 2012;2:2787–94. https://doi.org/10.1021/cs3005264.
[36] Kim BC, Manikandan R, Yu KH, Park MS, Kim DW, Park SY, et al. Efficient supercapattery behavior of mesoporous hydrous and anhydrous cobalt molybdate nanostructures. J Alloys Compd 2019;789:256–65. https://doi.org/10.1016/j.jallcom.2019.03.033.
[37] Ray SK, Dhakal D, Hur J, Lee SW. Morphologies controlled ZnO for inactivation of multidrug-resistant Pseudomonas aeruginosa in solar light. Nanotechnology 2020; 31. https://doi.org/10.1088/1361-6528/ab53bf.
[38] Eda K, Uno Y, Nagai N, Sotani N, Whittingham MS. Crystal structure of cobalt molybdate hydrate $CoMoO_4$· nH2O. J Solid State Chem 2005;178:2791–7. https://doi.org/10.1016/j.jssc.2005.06.014.
[39] Ding Y, Wan Y, Min Y-L, Zhang W, Yu S-H. General synthesis and phase control of metal molybdate hydrates $MMoO_4$·nH_2O (M = Co, Ni, Mn, n = 0, 3/4, 1) nano/microcrystals by a hydrothermal approach: magnetic, photocatalytic, and electrochemical properties. Inorg Chem 2008;47:7813–23. https://doi.org/10.1021/ic8007975.
[40] Wang Y, Yang L, Wang Y, Wang X, Han G. Morphology-controlled synthesis of PbMoO4 crystals by a simple. sonochemical method 2012;1:378–81.
[41] Abdulrahman AF, Ahmed SM, Hamad SM, Almessiere MA, Ahmed NM, Sajadi SM. Effect of different pH values on growth solutions for the ZnO nanostructures. Chin J Phys 2021;71:175–89. https://doi.org/10.1016/j.cjph.2021.02.013.
[42] Ray SK, Joshi B, Ramani S, Park S, Hur J. Multicolor and white light upconversion luminescence in α-NiMoO4:Yb3+/Ln3+ (Ln = Tm, Ho, Tm/Ho) nanoparticles. J Alloys Compd 2022;892:162101. https://doi.org/10.1016/j.jallcom.2021.162101.
[43] Thompson K, Choi J, Neupane D, Mishra SR, Perez F, Gupta RK. Tuning the electrochemical properties of nanostructured CoMoO4 and NiMoO4 via a facile sulfurization process for overall water splitting and supercapacitors. Surf Coating Technol 2021;421:127435. https://doi.org/10.1016/j.surfcoat.2021.127435.
[44] Ray SK, Dhakal D, Lee SW. Rapid degradation of naproxen by AgBr-α-NiMoO4 composite photocatalyst in visible light: mechanism and pathways. Chem Eng J 2018;347:836–48. https://doi.org/10.1016/j.cej.2018.04.165.
[45] Zhang X, Qin J, Xue Y, Yu P, Zhang B, Wang L, et al. Effect of aspect ratio and surface defects on the photocatalytic activity of ZnO nanorods. Sci Rep 2014;4: 4596. https://doi.org/10.1038/srep04596.
[46] Cheng X, Gao Q, Li K, Liu Z, Liu Q, Liu Q, et al. Enhanced phase transition properties of VO_2 thin films on 6H-SiC (0001) substrate prepared by pulsed laser deposition. Nanomaterials 2019;9:1–9. https://doi.org/10.3390/nano9081061.
[47] Moura AP de, Oliveira LH de, Pereira PFS, Rosa ILV, Li MS, Longo E, et al. Photoluminescent properties of CoMoO4 nanorods quickly synthesized and annealed in a domestic microwave oven. Adv Chem Eng Sci 2012;2:465–73. https://doi.org/10.4236/aces.2012.24057.
[48] Liu F, Yang Y, Li S, Chen T, Long H, Wang H, et al. Multi-dimensional CuO nanorods supported CoMoO4 nanosheets heterostructure as binder free and high stable electrode for supercapacitor. J Mater Sci Mater Electron 2018;29:10353–61. https://doi.org/10.1007/s10854-018-9092-2.
[49] Ray SK, Dhakal D, Regmi C, Yamaguchui T, Lee SW. Inactivation of Staphylococcus aureus in visible light by morphology tuned α-NiMoO4. J Photochem Photobiol Chem 2018;350:59–68. https://doi.org/10.1016/j.jphotochem.2017.09.042.
[50] Sezancoski JC, Bomio MDR, Cavalcante LS, Joya MR, Pizani PS, Varela JA, et al. Morphology and blue photoluminescence emission of PbMo04 processed in conventional hydrothermal. J Phys Chem C 2009;113:5812–22. https://doi.org/10.1021/jp810294q.
[51] Li W, Wang X, Hu Y, Sun L, Gao C, Zhang C, et al. Hydrothermal synthesized of comoo4 microspheres as excellent electrode material for supercapacitor. Nanoscale Res Lett 2018;13:1–10. https://doi.org/10.1186/s11671-018-2540-3.
[52] Wang X, Li W, Wang X, Zhang J, Sun L, Gao C, et al. Electrochemical properties of NiCoO2 synthesized by hydrothermal method. RSC Adv 2017;7:50753–9. https://doi.org/10.1039/c7ra10232a.
[53] Parveen N, Ansari SA, Alamri HR, Ansari MO, Khan Z, Cho MH. Facile synthesis of SnS2 nanostructures with different morphologies for high-performance supercapacitor applications. ACS Omega 2018;3:1581–8. https://doi.org/10.1021/acsomega.7b01939.
[54] Gao Z, Zeng Z, Xu X, Mao R, Jia R, Han S. Hollow nanotube arrays of CoP@CoMoO4 as advanced electrocatalyst for overall water splitting. Int J Hydrogen Energy 2023. https://doi.org/10.1016/j.ijhydene.2023.07.179.
[55] Zhou Y, Jin P, Zhou Y, Zhu Y. High-performance symmetric supercapacitors based on carbon nanotube/graphite nanofiber nanocomposites. Sci Rep 2018;8:1–7. https://doi.org/10.1038/s41598-018-27460-8.
[56] Xu X, Shen J, Li N, Ye M. Microwave-assisted synthesis of graphene/CoMoO4 nanocomposites with enhanced supercapacitor performance. J Alloys Compd 2014; 616:58–65. https://doi.org/10.1016/j.jallcom.2014.07.047.
[57] Mao X, Wang Y, Xiang C, Zhan D, Zhang H, Yan E, et al. Core-shell structured CuCo2S4@CoMoO4 nanorods for advanced electrode materials. J Alloys Compd 2020;844:156133. https://doi.org/10.1016/j.jallcom.2020.156133.
[58] Baskar S, Meyrick D, Ramakrishnan KS, Minakshi M. Facile and large scale combustion synthesis of α-CoMoO4: mimics the redox behavior of a battery in aqueous hybrid device. Chem Eng J 2014;253:502–7. https://doi.org/10.1016/j.cej.2014.05.068.
[59] Seevakan K, Manikandan A, Devendran P, Baykal A, Alagesan T. Electrochemical and magneto-optical properties of cobalt molybdate nano-catalyst as high-performance supercapacitor. Ceram Int 2018;44:17735–42. https://doi.org/10.1016/j.ceramint.2018.06.240.
[60] Zhang X, Yue L, Zhang S, Feng Y, An L, Wang M, et al. Nickel-doped cobalt molybdate nanorods with excellent cycle stability for aqueous asymmetric supercapacitor. Int J Hydrogen Energy 2020;45:8853–65. https://doi.org/10.1016/j.ijhydene.2020.01.127.
[61] Watcharatharapong T, Minakshi Sundaram M, Chakraborty S, Li D, Shafiullah GM, Aughterson RD, et al. Effect of transition metal cations on stability enhancement for molybdate-based hybrid supercapacitor. ACS Appl Mater Interfaces 2017;9: 17977–91. https://doi.org/10.1021/acsami.7b03836.
[62] Luo J, Wang X, Gu Y, Wang D, Wang S, Li W, et al. Constructing hollow nanocages of Co3O4-CoMoO4 heterostructure for efficient electrocatalytic oxygen evolution reaction. Appl Surf Sci 2022;606:154562. https://doi.org/10.1016/j.apsusc.2022.154562.
[63] Rani BJ, Swathi S, Yuvakkumar R, Ravi G, Kumar P, Babu ES, et al. Solvothermal synthesis of CoMoO4 nanostructures for electrochemical applications. J Mater Sci Mater Electron 2021;32:5989–6000. https://doi.org/10.1007/s10854-021-05319-5.
[64] Li Y, Wang C, Cui M, Chen S, Ma T. A novel strategy to synthesize CoMoO4 nanotube as highly efficient oxygen evolution reaction electrocatalyst. Catal Commun 2019;131:105800. https://doi.org/10.1016/j.catcom.2019.105800.
[65] Yang Y, Wang S, Jiang C, Lu Q, Tang Z, Wang X. Controlled synthesis of hollow Co-Mo mixed oxide nanostructures and their electrocatalytic and lithium storage properties. Chem Mater 2016;28:2417–23. https://doi.org/10.1021/acs.chemmater.6b00761.
[66] Zhang B, Liu G, Jin B, Zhao L, Lang X, Zhu Y, et al. CoMoO4/rGO hybrid structure embellished with Cu nanoparticles: an electrocatalyst rich in oxygen vacancies towards enhanced oxygen evolution reaction. Mater Lett 2021;293:129741. https://doi.org/10.1016/j.matlet.2021.129741.
[67] Xie W, Huang J, Huang L, Geng S, Song S, Tsiakaras P, et al. Novel fluorine-doped cobalt molybdate nanosheets with enriched oxygen-vacancies for improved oxygen evolution reaction activity. Appl Catal B Environ 2022;303:120871. https://doi.org/10.1016/j.apcatb.2021.120871.
[68] Zhang Y, Guo H, Yuan P, Pang K, Cao B, Wu X, et al. Structural evolution of CoMoO4 to CoOOH by ion electrochemical etching for boosting oxygen evolution reaction. J Power Sources 2019;442:227252. https://doi.org/10.1016/j.jpowsour.2019.227252.
[69] Liu H, Zhao D, Hu P, Chen K, Wu X, Xue D. Design strategies toward achieving high-performance CoMoO4@Co1.62Mo6S8 electrode materials. Mater Today Phys 2020;13. https://doi.org/10.1016/j.mtphys.2020.100197.
[70] Karmakar A, Senthamaraikannan TG, Baasanjav E, Bandyopadhyay P, Jin B, Park YS, et al. Surface hydroxyl group-enriched nickel cobalt molybdate hydrate for improved oxygen evolution activity in an anion exchange membrane water electrolyzer. Appl Catal B Environ 2023;328:122504. https://doi.org/10.1016/j.apcatb.2023.122504.